Significantly enhanced energy storage density of sandwich-structured $(Na_{0.5}Bi_{0.5})_{0.93}Ba_{0.07}TiO_3$/P(VDF-HFP) composites induced by PVP-modified two-dimensional platelets

Chao Jiang,[1,2] Dou Zhang,[1*] Kechao Zhou,[1] Xuefan Zhou,[1] Hang Luo,[1] and Isaac Abrahams [2*]

[1]State Key Laboratory of Powder Metallurgy, Central South University; Changsha 410083, China

[2] Materials Research Institute, School of Biological and Chemical Sciences, Queen Mary University of London, Mile End Road, London E1 4NS, UK

Corresponding Authors
Prof. D. Zhang
State Key Laboratory of Powder Metallurgy
Central South University
Changsha 410083, China
Email: dzhang@csu.edu.cn

I. Abrahams
School of Biological and Chemical Sciences
Queen Mary University of London
Mile End Road, London E1 4NS, UK
Email: i.abrahams@qmul.ac.uk

Abstract

Two-dimensional $(Na_{0.5}Bi_{0.5})_{0.93}Ba_{0.07}TiO_3$ (NBBT) platelets with a size of up to *ca*. 5 μm and thickness of 0.2-0.5 μm were introduced as fillers into a polymer matrix to prepare energy storage composites for the first time. The NBBT platelets were treated with an aqueous solution of H_2O_2 and coated with polyvinylprrolidone (PVP) before mixing with poly(vinylidene fluoride-co-hexafluoropropylene) (P(VDF-HFP)). The final composite was denoted as NBBT@PVP/P(VDF-HFP). Composites were prepared with NBBT@PVP loadings from 1 to 30 vol%. The relative permittivity of the composites increased significantly with increasing NBBT@PVP loading, while the breakdown strength decreased. To improve the breakdown strength of the composites, a sandwich-structure of multilayer films was developed, which used NBBT@PVP/ P(VDF-HFP) composites with 1 vol% NBBT loadings as central hard layers and the composites with 30 vol% NBBT loadings as neighboring soft layers. The five-layered film, which contained three central hard layers and neighboring soft layers, showed excellent energy storage properties. The breakdown strength and the maximum energy storage density of the film reached 258 $kV \cdot mm^{-1}$ and 14.95 $J \cdot cm^{-3}$, respectively. The energy efficiency remained 0.9 at an electric field of 200 $kV \cdot mm^{-1}$. The findings provide a new approach to produce energy storage materials with high performance.

1. Introduction

Capacitors play key roles in modern electrical and electronic systems, with both electrochemical and dielectric capacitors widely used. [1-5] Compared to electrochemical capacitors, dielectric capacitors have advantages due to their high charge and discharge speed (ms to μs) and an almost unlimited cycle life. [6] Traditionally, dielectric ceramic materials, such as lead zirconate titanate (PZT), [7] barium titanate ($BaTiO_3$), [8] and other relaxor ferroelectrics, [9,10] have been used to prepare dielectric capacitors. Despite their high permittivity, the energy storage densities (U) of these ceramics are limited due to their low breakdown strength (E_b). Their maximum energy densities (U_{max}) are described by **Equation 1**, [6,11,12]

$$U_{max} = \frac{\varepsilon_0 \varepsilon_r E_b^2}{2} \quad (1)$$

where ε_0 and ε_r are the vacuum and sample permittivities, respectively.

Therefore, to achieve high energy storage density, both high permittivity and large breakdown strength are required. Compared to ceramics, many polymers enjoy much higher breakdown strength, but exhibit much smaller permittivity. [13-15] Ceramic/polymer composites were therefore developed, with high permittivity resulting from the ceramic fillers and large breakdown strength from the polymer matrix. [16,17] The aforementioned ceramics have typically been used as the fillers, with poly(vinylidene fluoride) (PVDF) usually chosen as the polymer matrix, because of its large electric breakdown strength and relatively high relative permittivity. These ceramic/polymer composites show much higher energy storage densities than the pure dielectric ceramics. [18-21]

The morphology of the filler has been identified as an important factor in the energy storage densities of ceramic/polymer composites. [22-24] According to the effective medium theory, [25] the relative permittivity of the composite is determined by the depolarization factor, which itself is strongly dependent on the aspect ratios of the

ceramic fillers in the composite. Fillers with higher aspect ratios are more effective in enhancing the relative permittivity of composites at low concentration, compared to zero-dimensional fillers. Recently, Tang *et al.* [26] studied the effect of filler aspect ratio on the energy storage densities of composites containing PZT nanowires and nanorods with different aspect ratios. Their research showed that PZT nanowires of higher aspect ratio were more effective than those of lower aspect ratio in increasing energy density. Liu and Zhai [4] prepared surface-modified $SrTiO_3$ nanofibers, and proved that the one-dimensional ceramic fibers were highly effective in enhancing the relative permittivity of composites, compared to spherical fillers; their smaller specific surface helps to reduce the surface energy and thus limits the extent of agglomeration of the nanofillers in the polymer matrix. Similarly, the small specific surface of two-dimensional platelets with high aspect ratios, lower the surface energy compared to spherical particles, reducing agglomeration in the polymer matrix and the formation of conductive paths in the composites.

In this work, two-dimensional $(Na_{0.5}Bi_{0.5})_{0.93}Ba_{0.07}TiO_3$ (NBBT) platelets with high aspect ratios have, for the first time, been used as fillers to prepare composites. Two-dimensional ceramic fillers have specific advantages over spherical and one-dimensional ceramic fillers. Firstly, two-dimensional fillers have smaller specific surface area which can reduce the surface energy and the number of interfacial defects, and thus reduce agglomeration in the polymer matrix. Secondly, two-dimensional fillers can be easily textured using the tape casting technique. According to Andrews *et al.*, [27] the orientation of the fillers is critical for achieving high electromechanical coupling, which contributes significantly to the dielectric properties of the final composite.

Other research has focused on surface modification of the fillers. [28-30] Organic coatings onto the surface of the inorganic fillers facilitate their dispersion in the polymer matrix, which can not only reduce the aggregation of the fillers and interfacial defects between fillers and the matrix, but also provide a larger interfacial polarization. Niu *et al.* [11] studied the effect of the modifier structure on the performance of dielectric composites. Their research showed that the breakdown

strength of the composites was significantly improved by loading with coated fillers, which further led to the significant improvement of the energy storage densities of the composites. Considering the effect of surface modification of the dielectric fillers on the energy storage density of the final composite, the NBBT fillers used in this work were treated with an aqueous solution of H_2O_2 and coated with polyvinylpyrrolidone (PVP) before mixing with poly(vinylidene fluoride-co-hexafluoropropylene) (P(VDF-HFP)).

A third route to improving the energy-storage properties of polymer-based composites is through the use of layered constructions involving several composite layers, with different filler loadings. Wang *et al.* [31] showed that a $BaTiO_3$/PVDF composite, comprised of a central hard layer with 1 vol% $BaTiO_3$ loading and neighboring layers with 20 vol% $BaTiO_3$ loading, exhibited a dramatically improved breakdown strength and energy density, *i.e.* 470 $kV \cdot mm^{-1}$ and 18.8 $J \cdot cm^{-3}$, respectively. In this work, we propose a modified design for sandwich-structured multilayer films, using different NBBT loadings. The strong barrier interfaces that exist between adjacent layers in the sandwich structure protect the composite films from total breakdown and suppress the formation of conductive paths in the composites, contributing to much higher breakdown strengths than that of a single layer. [32,33] The large electric displacement polarization induced by the upper and lower surface layers, with high NBBT loading, guarantees a high dielectric maximum polarization and limits the remnant polarization of the composite films. As a result, a novel advanced energy storage material with excellent performance was achieved, providing a useful approach to exploit prospective dielectric candidates for energy-storage applications.

2. Experimental

The coating processes and the fabrication processes for the sandwich-structured multilayer films are summarized schematically in **Fig. 1.** NBBT platelets were synthesized by a topochemical reaction method using two-dimensional

$Na_{0.5}Bi_{4.5}Ti_4O_{15}$ (NBIT) as precursors. Firstly, NBIT was prepared from stoichiometric amounts of Bi_2O_3 (99.9%, Sinopharm Chemical Reagent Co., Ltd), TiO_2 (99.9%, Sinopharm Chemical Reagent Co., Ltd) and Na_2CO_3 (99.9%, Sinopharm Chemical Reagent Co., Ltd) using a molten salt synthesis method. The starting materials were mixed with an equal weight of NaCl and ball milled for 24 h in ethanol. The mixture was then dried at 60 °C. The dried mixture was then heated at 1050 °C for 4 h in a covered alumina crucible, before cooling in the furnace to room temperature. Secondly, stoichiometric amounts of NBIT, Na_2CO_3, $BaCO_3$ and TiO_2 were mixed with an equal weight of NaCl as a suspension in ethanol, with a magnetic stirrer at 60 °C and the ethanol evaporated. The dried mixture was placed in a covered alumina crucible at 950 °C for 6 h, before cooling to room temperature in the furnace. The product was washed with hot deionized water several times to remove the salt and dried at 80 °C for 24 h.[34] The as-synthesized NBBT platelets were then crushed in liquid nitrogen.

NBBT platelets (20 g) were added to an aqueous solution of H_2O_2 (100 ml, 30 wt %, Sinopharm Chemical Reagent Co., Ltd) in a round-bottomed flask. The mixture was sonicated for 30 min and refluxed at 106 ℃ for 6 h. The treated platelets were recovered by centrifugation at 9000 rpm for 5 min. The obtained NBBT platelets were washed with deionized water several times, with centrifugation at 1000 rpm and then dried under vacuum at 80 °C for 12 h. Subsequently, poly (vinyl pyrrolidone) (PVP, molecular weight 1300000 Da, Aldrich Chemistry) was dissolved in ethanol (PVP: 0.1 g and ethanol: 10 ml) and stirred at room temperature for 24 h, then mixed with NBBT platelets (10 g) pretreated with H_2O_2, followed by stirring for 48 h at 60 °C. The surface modified NBBT platelets were recovered by centrifuging at 2000 rpm for 2 min, washed several times with deionized water, and finally dried under vacuum at 80 ℃ for 24 h. The PVP coated NBBT platelets were ball-milled in N,N-dimethylformamide (DMF, Sinopharm Chemical Reagent Co., Ltd) for 2 days and mixed with P(VDF-HFP) (pellets with less than 15% HFP, Aldrich) for another 5 days by ball-milling. Three different suspensions were obtained which contained 1 vol%, 5 vol% and 30 vol% NBBT platelets, respectively. The suspensions were then

cast onto clean glass and dried at 80 °C for 12 h under vacuum. The thickness of the dried composites was around 10 μm.

Three kinds of sandwich-structured multilayer films were prepared containing several central hard layers (1 vol% NBBT loaded, denoted "1") and neighboring soft layers (30 vol% NBBT loaded, denoted "30"). Multilayer films of 3 ("30-1-30"), 5 ("30-1-1-1-30") and 7 layers ("30-30-1-1-1-30-30") were compressed by hot-pressing 1 MPa at 200 °C for 0.5 h.

Transmission electron microscopy (TEM) images were obtained using a JEOL JEM-2100 instrument operated at an accelerating voltage at 200 kV. The morphologies of the composites were examined by scanning electron microscopy (SEM, JSM-6390). X-ray powder diffraction data were collected in θ/2θ mode using a Rigaku D-Max/2550VB+ diffractometer with Cu Kα radiation (λ = 1.5418 Å). Rietveld analysis of the X-ray powder diffraction data was carried out using the GSAS [35] suite of programs, using the structures reported by Blanchard *et al.* [36] and Jones and Thomas, [37] for the monoclinic and tetragonal polymorphs of $Na_{0.5}Bi_{0.5}TiO_3$, respectively, as starting models, with appropriate substitution of Na/Bi by Ba.

For measurement of dielectric properties, gold electrodes of about 50 nm in thickness were sputtered on both sides of the films using a mask with 1 mm diameter eyelets. Frequency-dependent relative permittivity and dielectric loss were measured using an Agilent 4294A LCR meter, over the frequency range 1 kHz to 10 MHz. Displacement-electric field (*D-E*) loops were measured using a Precision Premier II ferroelectric polarization tester (Radiant, Inc.) at room temperature at a frequency of 100 Hz. Electric breakdown strength was tested using the Dielectric Withstand Voltage Test (Beijing Electro-mechanical Research Institute Supesvoltage Technique) at a ramp rate of 200 V s^{-1} and a limit current of 5 mA. The voltage was increased gradually until breakdown occurred. Five different points were measured for every sample.

3. Results and discussion

3.1 Characterization of the NBBT platelets and NBBT@PVP/P(VDF-HFP) composites

Fig. 2 shows the fitted X-ray powder diffraction (XRD) pattern of the NBBT platelets. Close inspection of the data (**Fig. 2 inset**), reveals two sets of peaks, a major phase, which was best modelled as a monoclinic phase in space group *Cc* and a minor tetragonal phase in space group *P*4*bm*, with refined weight fractions of 0.775(2) and 0.225(5), respectively. The structural and refinement parameters are summarized in **Table 1**. The monoclinic phase has a higher density than the tetragonal phase, which is reflected in a smaller perovskite cell volume of 59.36 $Å^3$ compared to the tetragonal phase with a value of 59.77 $Å^3$. Significant preferred orientation is evident, in the monoclinic phase, consistent with platelet morphology. The SEM image in **Fig. 3a**, confirms the platelet morphology, revealing high aspect ratios, with platelet dimensions of up to *ca*. 5 μm and thicknesses of 0.2-0.5 μm. **Fig. 3b** shows a transmission electron microscopy (TEM) bright field image illustrating the morphology and distribution of ferroelectric domains, where the dark and bright fringes represent the domains, with the domains and domain boundaries, typical of ferroelectric materials, [38] clearly observed in the piezoelectric force microscopy (PFM) image **(Fig. 3c**).

Fig. 4a and **4b** show TEM bright field and high resolution images of the PVP coated NBBT, respectively. A resin layer is clearly observed on the surface of a NBBT platelet and is marked by two parallel lines in **Fig. 4b**. The NBBT platelets were treated with H_2O_2 before reacting with PVP, because neat NBBT platelets lack reactive functional groups on their surface, e.g., -OH, and it is difficult to form chemical bonds with the PVP coating. [18] The morphology of the NBBT@PVP/P(VDF-HFP) composites observed by TEM are shown in **Fig. 4c** and **4d**. It can be seen that the surface modified platelets were successfully dispersed into the polymer matrix. There were no obvious interfacial defects between the platelets and the P(VDF-HFP) matrix, revealing excellent compatibility between them, which is seen as a critical factor in ensuring high breakdown strength in the ceramic/polymer composite. **Fig. 5** shows mapping images of a NBBT@PVP/P(VDF-HFP) film

scanned using an energy dispersive spectrometer in SEM mapping mode and confirms a uniform distribution of the constituent elements.

Fig. 6 shows the XRD patterns of pure PVP/P(VDF-HFP) and NBBT@PVP/P(VDF-HFP) composites with NBBT loadings of 1, 5 and 30 vol%. It can be seen that all the XRD patterns of the NBBT@PVP/P(VDF-HFP) composites exhibit an intense scattering background and a broad feature at about 20° 2θ, which is attributable to the amorphous structure of pure PVP/P(VDF-HFP). All patterns for NBBT@PVP/P(VDF-HFP) composites show Bragg peaks corresponding to both the monoclinic and tetragonal polymorphs, with even greater preferred orientation compared to the neat platelets (**Fig. 2**). The changes in relative intensity of the peaks associated with the two phases suggest that the monoclinic phase becomes more dominant with increasing NBBT loading, suggesting a preference for this phase in the tape casting process. The orientation degree for the composite can be estimated by the Lotgering factor *f*, [39,40] which was calculated as about 0.7 for the 30 vol% loaded sample. The high preferred orientation indicated that most NBBT platelets in the composites were parallel to each other, due to the effect of the shearing force during the tape casting process.

Fig. 7a shows the dielectric properties of pure P(VDF-HFP) and NBBT@PVP/P(VDF-HFP) composites with various NBBT loadings as a function of frequency, over the range 1 kHz to 10 MHz. It can be seen that relative permittivity decreases slightly above 100 kHz, while significant increases in relative permittivity are seen with increasing NBBT loading. The highest values for relative permittivity were seen for the 30 vol% loaded sample, ranging from 34.1 at 1 kHz to 31.3 at 10 MHz. The dielectric losses of pure P(VDF-HFP) and all the three composites (**Fig. 7b**) remained low and stable over the frequency range 1 to 100 kHz, at which point there was a significant increase in dielectric loss caused by the α_a relaxation of the P(VDF-HFP) matrix. [12, 41-44] At low frequencies, the highest dielectric loss is exhibited by the sample with the highest loading, while at frequencies above 100 kHz, the trend is reversed and the sample with the lowest loading shows the highest dielectric loss. The low dielectric loss of the composites at lower frequencies can be attributed to

several factors, including the insulating PVP shells on the surfaces of the NBBT platelets, homogeneous dispersion of the platelets in the P(VDF-HFP) matrix and the isotactic structure of the P(VDF-HFP) matrix due to addition of two-dimensional fillers. The high dielectric loss of the composites at higher frequencies can be attributed to the contribution of the dielectric loss of the P(VDF-HFP) matrix, which is increased significantly due to the α_a relaxation of the P(VDF-HFP) matrix when the frequency exceeds a critical value. At low frequencies, the dielectric loss of NBBT is much higher than that of pure P(VDF-HFP), so the composite with higher NBBT loading has the higher dielectric loss, due to the contribution of the NBBT fillers to the total dielectric loss of the composites. However, when the frequency exceeds a critical value, the dielectric loss of the P(VDF-HFP) matrix contributes much more to the dielectric loss of the composites, so the composite with lower NBBT loading has the higher dielectric loss.

The energy density of the composites can be calculated from the displacement-electric field (*D-E*) loops using **Equation 2**.

$$U = \int E \, dD \tag{2}$$

where E is the electric field and D is the electric displacement and is given by **Equation 3**: [6,12]

$$D = \varepsilon_0 \, \varepsilon_r \, E \tag{3}$$

Typical *D-E* loops of the pure P(VDF-HFP) and NBBT@PVP/P(VDF-HFP) composites for various NBBT loadings are shown in **Fig. 7c**. With increasing NBBT loading, electric displacement increased notably under the same electric field. The maximum displacement of pure P(VDF-HFP) was 0.89 $\mu C \cdot cm^{-2}$ under an electric field of 100 $kV \cdot mm^{-1}$ and increased to 7.51 $\mu C \cdot cm^{-2}$ for the composite with 30 vol % NBBT under the same electric field. The increased displacement is attributable to the

increase in relative permittivity of the composites. The breakdown strength decreases with increasing NBBT loading (**Fig. 7d**), with values of 390 kV·mm^{-1} for pure P(VDF-HFP), decreasing to 185 kV·mm^{-1} at 30 vol% NBBT loading. This phenomenon has been attributed not only to the low breakdown strength of the ceramic fillers themselves, but also to the presence of three-dimensional percolating networks due to addition of a large amount of ceramic filler, which forms a conductive pathway in the polymer matrix and leads to a decrease of the effective breakdown strength of the composites. [33,45]

The energy densities of the samples as a function of electric field are shown in **Fig. 8a**. As can be seen, the energy densities of the samples increased with increasing electric field. For example, the energy density of the sample with 30 vol% NBBT increased from 2.2 × 10^{-4} J·cm^{-3} at 1 kV·mm^{-1} to 2.21 J·cm^{-3} at 100 kV·mm^{-1}. The energy density also increased significantly with increasing NBBT loading, showing an increase of around 400% between the pure P(VDF-HFP) and the 30 vol% loaded sample (0.47 J·cm^{-3} and 2.21 J·cm^{-3} at 100 kV·mm^{-1}, respectively). The maximum energy density (U_{max}) of the samples can be estimated using **Equation 1**. For pure P(VDF-HFP), the value of the maximum energy density was found to be 4.06 J·cm^{-3} (**Fig. 8b**). Although the breakdown strength of the composite with 30 vol% NBBT decreased to 187 kV·mm^{-1}, the energy density still increased to 7.64 J·cm^{-3}, owing to its high relative permittivity of 34.1. This maximum energy density value is significantly higher than that for pure P(VDF-HFP). Energy efficiency is another important factor to be assessed for practical applications, since the energy losses often lead to heating and degradation of performance and reliability of the materials. The energy efficiency (η) can be calculated using **Equation 4**.

$$\eta = \frac{U}{U + U_{loss}} \tag{4}$$

where U_{loss} is the energy density loss of the composites as calculated from the D-E loops. The calculated energy efficiencies of the composites at an electric field of 150

$kV \cdot mm^{-1}$ are shown in **Fig. 8b**. As the NBBT loading increased from 0 vol% (pure P(VDF-HFP)) to 30 vol%, the energy efficiency decreased gradually from 0.937 to 0.485. This again is attributed to the formation of three-dimensional percolating networks resulting in conductive pathways in the polymer matrix. [33]

3.2 Characterization of sandwich-structured multilayer NBBT@PVP/P(VDF-HFP) films

Sandwich structured multilayer films were constructed by hot pressing 1 vol% and 30 vol% NBBT loaded monolayers. Three types of multilayer films were produced and designated according to the loading level of the component monolayers as "30-1-30", "30-1-1-1-30" and "30-30-1-1-1-30-30" for the 3, 5 and 7 layer films, respectively. The cross-sectional morphologies of a monolayer NBBT@PVP/P(VDF-HFP) composite and the three kinds of sandwich-structured multilayer films are shown in the SEM images in **Fig. 9**, where the multilayer structure and the boundary lines between different layers are clearly observed. Compared to the monolayer composite, individual layers in the multilayer films are more compressed and their thicknesses are visibly reduced due to the effect of the hot pressing process.

Fig. 10a shows the dielectric properties of the studied sandwich-structured multilayer films as a function of frequency, over the range of 1 kHz to 10 MHz. For all three films, the relative permittivity shows a small decrease at frequencies over 100 kHz. It can be seen that the film "30-30-1-1-1-30-30" exhibited the highest relative permittivity, while the film "30-1-1-1-30" had the lowest values. Supposing that each layer in the multilayer films made their proportional contributions to the relative permittivity based on their thickness, the weighted average values of the relative permittivity for the films "30-1-30", "30-1-1-1-30" and "30-30-1-1-1-30-30" were calculated to be 25.30, 18.00 and 24.02, respectively. The significantly lower permittivity of the 30-1-1-1-30 film and closeness to each other of the values for the two other films is reflected in the observed data. The observed values of relative permittivity are all significantly higher than those calculated, being much closer to the values observed in the 30 vol% NBBT loaded monolayer. The results suggest that it is

the soft surface layers, not the central hard layers that make the major contribution to the relative permittivity in the multilayer films. As seen in the monolayers, the dielectric loss of the multilayer films (**Fig. 10b**) remained low and stable over the frequency range 1 to 100 kHz, but then stepped up at around 100 kHz. The 7-layer film shows the highest dielectric loss at 1 kHz, but shows the lowest dielectric loss at frequencies above *ca*. 100 kHz. The low dielectric loss of the films at lower frequencies can be attributed to the low dielectric loss of individual layers and the uniform interfaces in the unique sandwich structure, which interrupt the conductive paths at lower frequencies. The high dielectric loss of the films at higher frequencies can be attributed to the contribution of the dielectric loss of the P(VDF-HFP) matrix, which is increased significantly, due to α_a relaxation, when the frequency exceeds a critical value.

Typical *D*-*E* loops of the three multilayer films are shown in **Fig. 10c**. It is seen that there are only small differences in the electric displacement between the three studied films. The extent of hysteresis reflects the relative contributions of the component layers. The "30-30-1-1-1-30-30" film shows the largest displacement among the three films under the same electric field, with the smallest displacement seen in the "30-1-1-1-30" film. The maximum displacements for the films"30-30-1-1-1-30-30", "30-1-30" and "30-1-1-1-30" are 9.75 $\mu C \cdot cm^{-2}$, 9.08 $\mu C \cdot cm^{-2}$ and 8.48 $\mu C \cdot cm^{-2}$, respectively. To calculate the maximum energy densities of the films, the breakdown strengths were measured, as shown in **Fig. 10d**. The "30-1-1-1-30" film shows the largest breakdown strength, which reaches 258 $kV \cdot mm^{-1}$, while the "30-1-30" film has the lowest value of 217 $kV \cdot mm^{-1}$. In a similar way to the calculation of relative permittivity, the weighted average breakdown strength for the films "30-1-30", "30-1-1-1-30" and "30-30-1-1-1-30-30" were calculated to be 229, 262 and 234 $kV \cdot mm^{-1}$, respectively. The values are in reasonable agreement with those observed. The results demonstrate that it is possible to design a composite with a relative permittivity dominated by the contribution of the soft component and a dielectric loss reflecting a simple weighted combination of the contributions of individual layers.

The energy densities of the films as a function of electric field are shown in **Fig. 11a**. As can be seen, the energy densities for all three films increased with increasing electric field. For example, the energy density of the "30-1-30" film increased from 0.0249 $J \cdot cm^{-3}$ at 10 $kV \cdot mm^{-1}$ to 9.95 $J \cdot cm^{-3}$ at 200 $kV \cdot mm^{-1}$. The maximum energy density of the films "30-1-30", "30-1-1-1-30" and "30-30-1-1-1-30-30" were 11.45, 14.95 and 12.79 $J \cdot cm^{-3}$, respectively (**Fig. 11b**). The high energy densities of the films are attributable to the combination of high relative permittivity and high dielectric strength of the component monolayers. The former derives from the top and bottom soft layers (30 vol% NBBT loading), while the latter mainly comes from the central hard layers (1 vol% NBBT loading). The central hard layers act as electron traps which limit electron tunneling through the film resulting in improved breakdown strength. The calculated energy efficiencies of the three films at an electric field of 200 $kV \cdot mm^{-1}$ are shown in **Fig. 11b**. The film "30-1-1-1-30" had the highest energy efficiency among the three films, which reached as high as 0.9, while the other two films showed lower energy efficiencies of less than 0.8. These values are slightly lower than that of the unloaded P(VDF-HFP) matrix, which exhibits an energy efficiency of 93.64%. [12] The values of relative permittivity, dielectric loss, breakdown strength and energy density of the 5-layer composite prepared in the present study are comparable with those of other known composites (**Table 2**). [12, 4, 31]

4. Conclusions

A newly designed dielectric composite, which employs two-dimensional NBBT platelets, with high aspect ratios as filler, has been developed. Composites were successfully prepared containing NBBT loadings of up to 30 vol% NBBT. The breakdown strength of the composites decreased significantly with increase in NBBT loading. To improve the breakdown strength of NBBT@PVP/P(VDF-HFP) composites, sandwich-structured multilayer films were designed, which used 1 vol% NBBT loaded composite as central hard layers and 30 vol% NBBT loaded composite as neighboring soft layers. The design yielded films which exhibited relative

permittivities dominated by that of the soft layers, but with dielectric loss effectively a sum of contributions from individual layers. A five-layer film composed of three central hard layers sandwiched between single soft layers gave the best balance of features from the hard and soft layers. It showed excellent energy storage properties, with breakdown strength, energy storage density and energy efficiency values of 258 $kV \cdot mm^{-1}$, 14.95 $J \cdot cm^{-3}$ and 0.9, respectively.

Acknowledgments

This work was financially supported by Hunan Nonferrous Research Funding (grant no: YSZN2013CL05), Hunan Doctoral Research Innovation Project (grant no: CX2014B055), China Scholarship Council Joint Ph.D. Program (grant no: 201506370175) and the State Key Laboratory of Powder Metallurgy, Central South University, Changsha, China.

References

1 P. J. Hall, M. Mirzaeian, S. I. Fletcher, F. B. Sillars, A. J. R. Rennie, G. O. Shitta-Bey, G. Wilson, A. Cruden and R. Carter, *Energy Environ. Sci.*, 2010, **3**, 1238-1251.

2 P. Simon and Y. Gogotsi, *Nat. Mater.*, 2008, **7**, 845-854.

3 S. Liu, S. Xue, W. Zhang, J. Zhai and G. Chen, *J. Mater. Chem. A*, 2014, **2**, 18040-18046.

4 S. Liu and J. Zhai, *J. Mater. Chem. A*, 2015, **3**, 1511-1517.

5 H. R. Jo and C. S. Lynch, *J. Appl. Phys.*, 2016, **119**, 024104.

6 B. Chu, X. Zhou, K. Ren, B. Neese, M. Lin, Q. Wang, F. Bauer and Q. M. Zhang, *Science*, 2006, **313**, 334-336.

7 K. K. Uprety, L. E. Ocola and O. Auciello, *J. Appl. Phys.*, 2007, **102**, 084107.

8 S. Chao and F. Dogan, *Mater. Lett.*, 2011, **65**, 978-981.

9 W. P. Cao, W. L. Li, X. F. Dai, T. D. Zhang, J. Sheng, Y. F. Hou and W. D. Fei, *J. Eur. Ceram. Soc.*, 2016, **36**, 593-600.

10 Y. J. Kim, M. H. Park, Y. H. Lee, H. J. Kim, W. Jeon, T. Moon, K. Do Kim, D. S. Jeong, H. Yamada and C. S. Hwang, *Sci. Rep.*, 2016, **6**, 19039.

11 Y. Niu, Y. Bai, K. Yu, Y. Wang, F. Xiang and H. Wang, *ACS Appl. Mater. Interfaces*, 2015, **7**, 24168-24176.

12 H. Luo, D. Zhang, C. Jiang, X. Yuan, C. Chen and K. Zhou, *ACS Appl. Mater. Interfaces*, 2015, **7**, 8061-8069.

13 Q. Chen, B. J. Chu, X. Zhou and Q. M. Zhang, *Appl. Phys. Lett.*, 2007, **91**, 062907.

14 Z. M. Dang, J. K. Yuan, S. H. Yao and R. J. Liao, *Adv. Mater.*, 2013, **25**, 6334-6365.

15 P. H. Hu, Y. Song, H. Y. Liu, Y. Shen, Y. H. Lin and C. W. Nan, *J. Mater. Chem. A*, 2013, **1**, 1688-1693.

16 X. Zhang, Y. Shen, B. Xu, Q. Zhang, L. Gu, J. Jiang, J. Ma, Y. Lin, C.-W. Nan, *Adv. Mater.*, 2016, **28**, 2055-2061.

17 Q. Li, K. Han, M. R. Gadinski, G. Zhang, Q. Wang, *Adv. Mater.*, 2014, **26**, 6244-6249.

18 Y. Feng, W. L. Li, J. P. Wang, J. H. Yin and W. D. Fei, *J. Mater. Chem. A*, 2015, **3**, 20313-20321.

19 L. Xie, X. Huang, K. Yang, S. Li and P. Jiang, *J. Mater. Chem. A*, 2014, **2**, 5244-5251.

20 Prateek, V. K. Thakur and R. K. Gupta, *Chem. Rev.*, 2016, **116**, 4260-4317.

21 P. Hu, Y. Song, H. Liu, Y. Shen, Y. Lin and C.-W. Nan, *J. Mater. Chem. A*, 2013, **1**, 1688-1693.

22 Y. Feng, W. L. Li, Y. F. Hou, Y. Yu, W. P. Cao, T. D. Zhang and W. D. Fei, *J. Mater. Chem. C*, 2015, **3**, 1250-1260.

23 H. Tang, Z. Zhou and H. A. Sodano, *ACS Appl. Mater. Interfaces*, 2014, **6**, 5450-5455.

24 J. Feenstra and H. A. Sodano, *J. Appl. Phys.*, 2008, **103**, 124108.

25 T. C. Choy, *Effective medium theory: principles and applications*, Oxford University Press, 2015.

26 H. Tang, Y. Lin, C. Andrews and H. A. Sodano, *Nanotechnology*, 2011, **22**, 015702.

27 C. Andrews, Y. Lin and H. A. Sodano, *Smart Mater. Struct.*, 2010, **19**, 025018.K.

28 S. H. Liu, J. W. Zhai, J. W. Wang, S. X. Xue and W. Q. Zhang, *ACS Appl. Mater. Interfaces*, 2014, **6**, 1533-1540.

29 X. Huang and P. Jiang, *Adv. Mater.*, 2015, **27**, 546-554.

30 K. Yang, X. Y. Huang, Y. H. Huang, L. Y. Xie and P. K. Jiang, *Chem. Mater.*, 2013, **25**, 2327-2338.

31 Y. Wang, J. Cui, Q. Yuan, Y. Niu, Y. Bai and H. Wang, *Adv. Mater.*, 2015, **27**, 6658-6663.

32 P. Hu, Y. Shen, Y. Guan, X. Zhang, Y. Lin, Q. Zhang and C.-W. Nan, *Adv. Funct. Mater.*, 2014, **24**, 3172-3178.

33 P. Hu, J. Wang, Y. Shen, Y. Guan, Y. Lin and C.-W. Nan, *J. Mater. Chem. A*, 2013, **1**, 12321-12326.

34 C. Jiang, X. Zhou, K. Zhou, C. Chen, H. Luo, X. Yuan and D. Zhang, *J. Eur. Ceram. Soc.*, 2016, **36**, 1377-1383.

35 A. C. Larson, R. B. Von Dreele, *Los Alamos National Laboratory Report*, No. LAUR-86-748, (1987).

36 P.E.R. Blanchard, S. Liu, B.J. Kennedy, C.D. Ling, Z. Zhang, M. Avdeev, L.Y. Jang, J.F. Lee, C.W. Pao, J.L. Chen, *Dalton Trans*., 2014, **43**, 17358-17365.

37 G. O. Jones and P. A. Thomas, *Acta Crystallogr*., 2002, **B58**, 168-178.

38 R. Dittmer, W. Jo, J. Roedel, S. Kalinin and N. Balke, *Adv. Funct. Mater.*, 2012, **22**, 4208-4215.

39 F. K. Lotgering, *J. Inorg. Nucl. Chem.*, 1959, **9**, 113-123.

40 C. Jiang, K. Zhou, X. Zhou, Z. Li and D. Zhang, *Ceram. Int.*, 2015, **41**, 6858-6862.

41 H. M. Jung, J.-H. Kang, S. Y. Yang, J. C. Won and Y. S. Kim, *Chem. Mater.*, 2010, **22**, 450-456.

42 S. Wu, W. Li, M. Lin, Q. Burlingame, Q. Chen, A. Payzant, K. Xiao and Q. M.

Zhang, *Adv. Mater.*, 2013, **25**, 1734-1738.

43 N. Hirose and A. R. West, *J. Am. Ceram. Soc.*, 1996, **79**, 1633-1641.

44 M. P. McNeal, S. J. Jang and R. E. Newnham, *J. Appl. Phys.*, 1998, **83**, 3288.

45 H. Tang, Y. Lin and H. A. Sodano, *Adv. Energy Mater.*, 2012, **2**, 469-476.

Table 1 Crystal and refinement parameters for NBBT platelets. Estimated standard deviations are given in parentheses.

	Major phase	**Minor Phase**
Formula	$Na_{0.465}Bi_{0.465}Ba_{0.07}TiO_3$	$Na_{0.465}Bi_{0.465}Ba_{0.07}TiO_3$
M_r (g mol^{-1})	213.38	213.38
Crystal System	Monoclinic	Tetragonal
Space Group	*Cc*	*P*4*bm*
Cell Dimensions	a = 9.528(2) Å, b = 5.502(1) Å, c = 5.532(2) Å, β = 125.05(1)°	a = 5.5034(6) Å, b = 3.9468(5) Å
Volume (Å^3)	237.43(5)	119.54(3)
Z	4	2
D_{calc} (g cm^{-3})	5.969	5.928
Weight fraction	0.775(2)	0.225(5)
Appearance	Yellow platelets	
Preferred orientation	1 0 0	None
Data range refined	20-80° 2θ	
R-factors	R_{wp} = 0.1257, R_p = 0.0965, R_{ex} = 0.0982, R_F2 = 0.1410	
χ^2	1.654	
No of variables	28	
No of data points	2999	
No of reflections	208	

Table 2. Comparison of relative permittivity, dielectric loss, breakdown strength and energy density for different dielectric composites

Composite	**Relative permittivity (ε, at 1 kHz)**	**Dielectric loss (tanδ, at 1 kHz)**	**Breakdown strength (E_b, kV·mm^{-1})**	**Energy density (U_{max}, J·cm^{-3})**	**reference**
P(VDF-HFP) nanocomposites doped with $BaTiO_3$	48.9	0.065	330	8.13	12
PVDF composite doped with $SrTiO_3$ nanofibers	14.9	0.015	380	6.8	4
Sandwich-Structured $BaTiO_3$/PVDF Nanocomposites	35	< 0.05	470	18.8	31
5-layer aandwich-structured P(VDF-HFP) composites doped with two dimensional NBBT platelets	25.30	< 0.05	258	14.95	This paper

Figure captions

Fig. 1 Schematic illustrations of (a) the modification processes of the NBBT platelets and (b) the fabrication processes of PVP@ NBBT/ P(VDF-HFP) composites and the sandwich-structured multilayer films.

Fig. 2 Fitted X-ray diffraction profile for NBBT platelets showing observed (points) calculated (line) and difference (lower) profiles, with detail of the fit inset. Reflection positions are indicated by markers: monoclinic phase (lower) and tetragonal phase (upper).

Fig. 3 (a) SEM image showing platelet morphology; (b) TEM bright field image showing domain structure and (c) PFM image where the dark and bright fringes show individual domains.

Fig. 4 TEM images: a) bright field and b) high resolution images of a PVP coated NBBT platelet, the PVP layer on the surface of the NBBT platelet is marked by two lines which shows the thickness of the layer is about 5 nm; c) and d) bright field images of a NBBT@PVP/P(VDF-HFP) composite.

Fig. 5 EDS element mapping images of a NBBT@PVP/P(VDF-HFP) composite.

Fig. 6 XRD patterns of pure P(VDF-HFP) and NBBT@PVP/P(VDF-HFP) composites with different NBBT loadings of 1, 5 and 30 vol%.

Fig. 7 Frequency dependence of (a) relative permittivity and (b) dielectric loss; (c) *D-E* loops and (d) the breakdown strength for pure P(VDF-HFP) and NBBT@PVP/P(VDF-HFP) composites with 1, 5 and 30 vol% NBBT loadings.

Fig. 8 Energy storage properties for pure P(VDF-HFP) and NBBT@PVP/P(VDF-HFP) composites with 1, 5 and 30 vol% NBBT loadings: (a) variation of energy density with electric field and (b) variation of maximum energy density and energy efficiency at 150 kV mm^{-1} with NBBT loading.

Fig. 9 Cross sectional SEM images of (a) a NBBT@PVP/P(VDF-HFP) monolayer composite, (b) a three-layer "30-1-30" film, (c) a five-layer "30-1-1-1-30" film and (d) a seven-layer "30-30-1-1-1-30-30" film.

Fig. 10 Frequency dependence of (a) relative permittivity and (b) dielectric loss; (c) *D-E* loops and (d) the breakdown strength for multilayer NBBT@PVP/P(VDF-HFP) films.

Fig. 11 Energy storage properties of multilayer NBBT@PVP/P(VDF-HFP) films. The dependence of the energy densities on varying electric field, (a) variation of energy density with electric field and (b) variation of maximum energy density and energy efficiency at 200 kV mm^{-1} with layering.

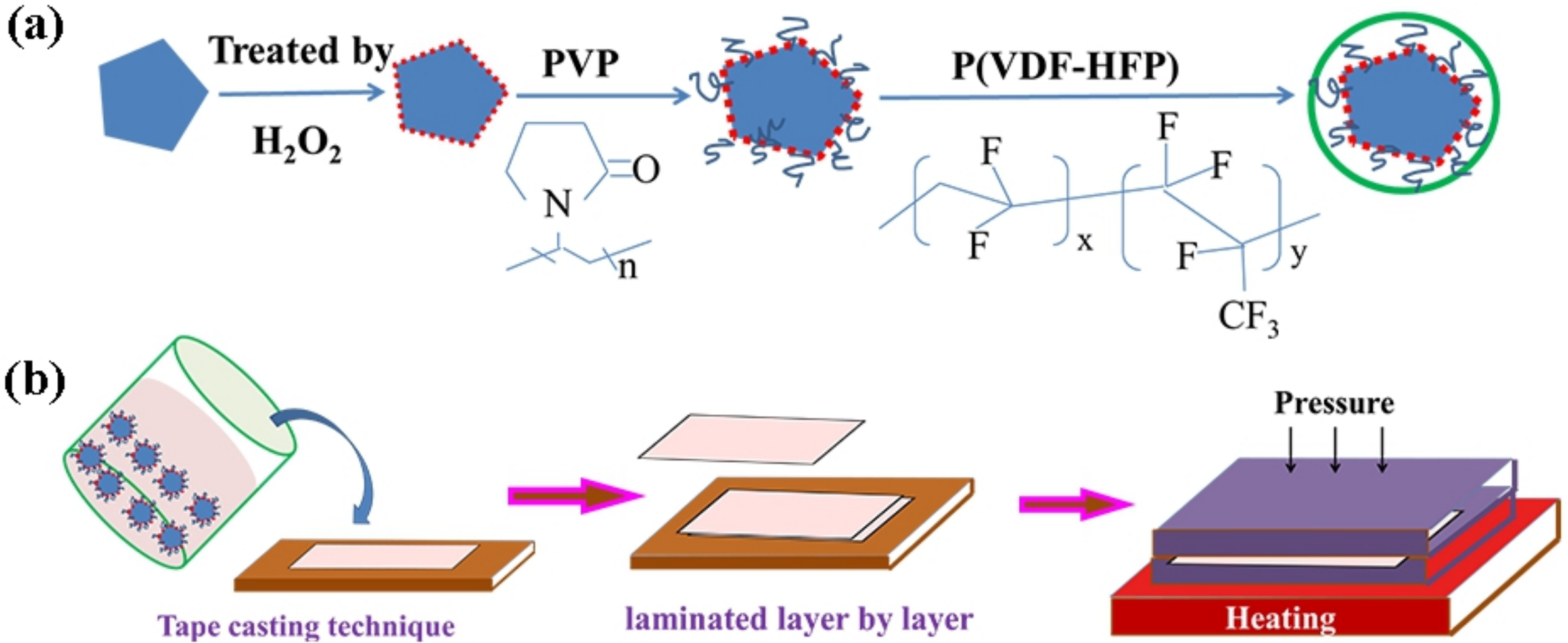
(a)
Treated by
H_2O_2
PVP
P(VDF-HFP)
O
N
n
F
F
x
F
F
F
y
CF_3
(b)
Pressure
Heating
Tape casting technique
laminated layer by layer

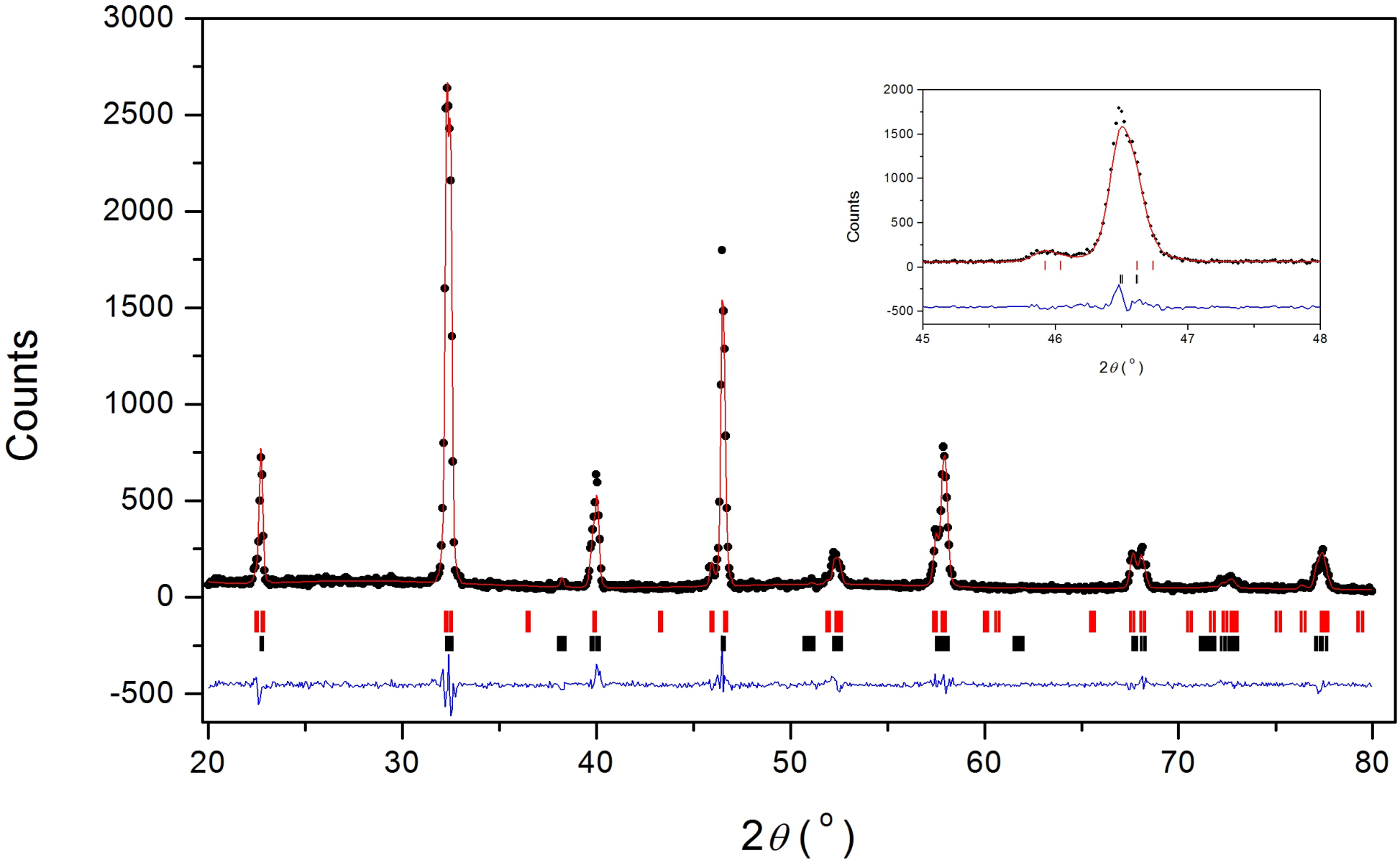
Counts
3000
2500
2000
1500
1000
500
0
-500
20
30
40
50
60
70
80
2θ(°)
Counts
2000
1500
1000
500
0
-500
45
46
47
48
2θ(°)

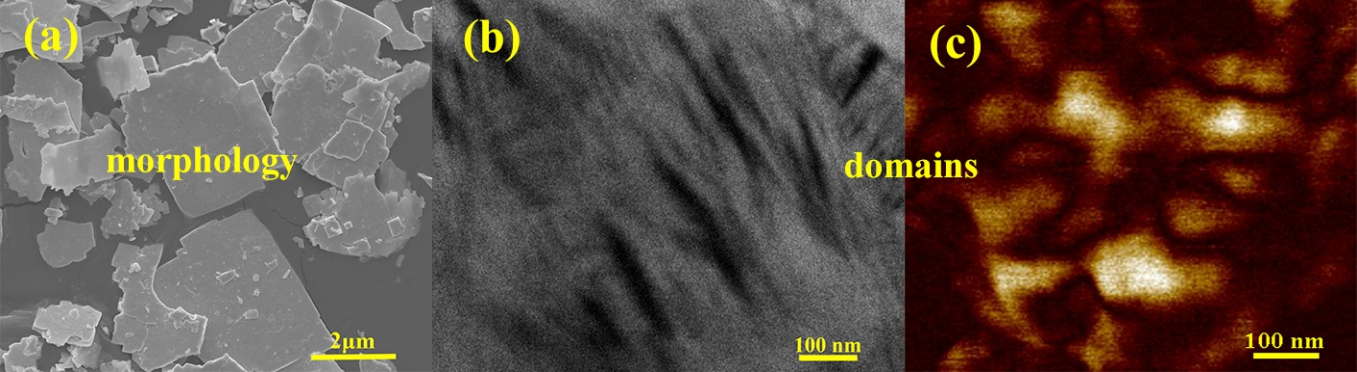
(a)
morphology
2μm
(b)
domains
100 nm
(c)
100 nm

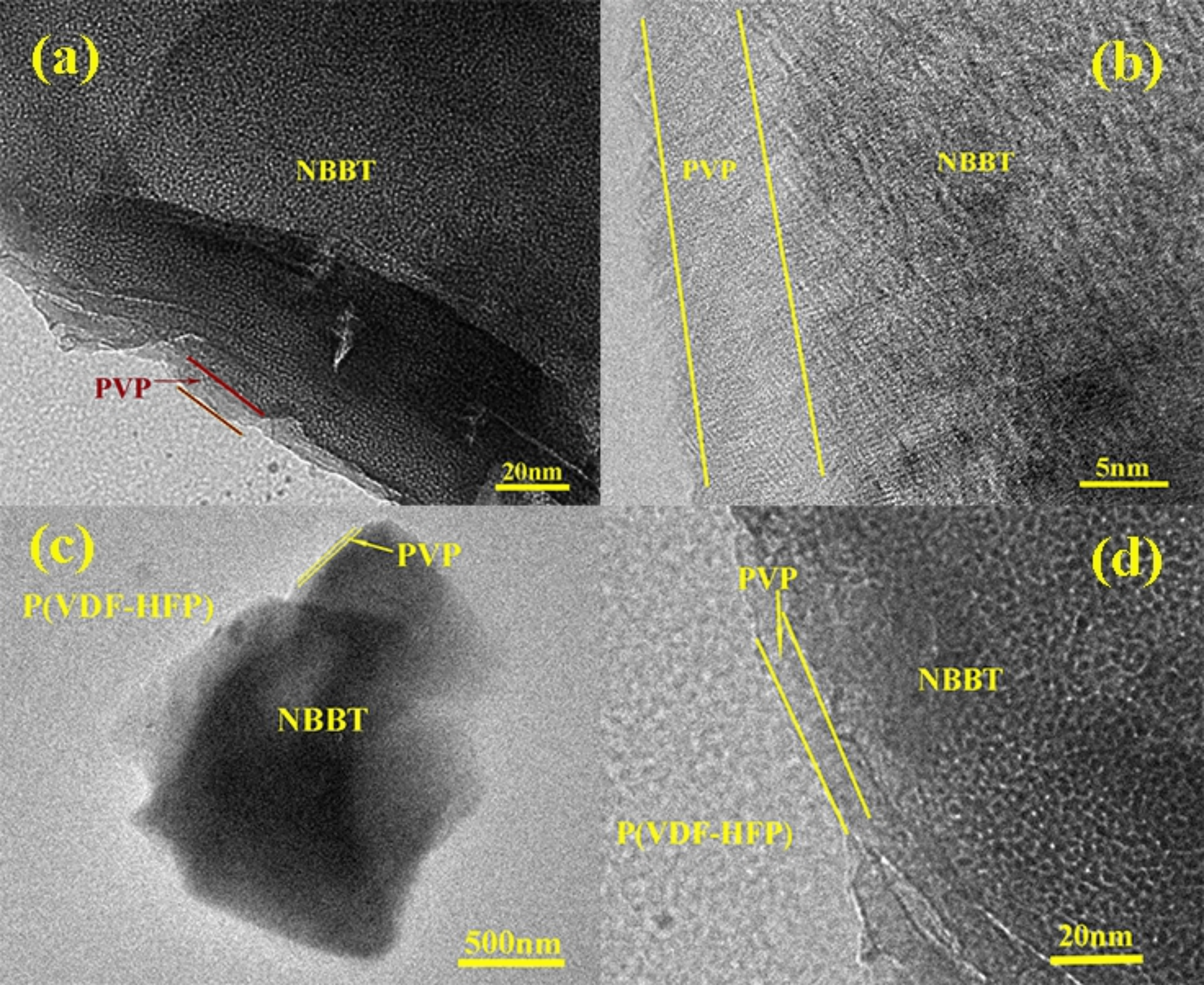
(a)
NBBT
PVP
20nm
(b)
PVP
NBBT
5nm
(c)
PVP
P(VDF-HFP)
NBBT
500nm
(d)
PVP
NBBT
P(VDF-HFP)
20nm

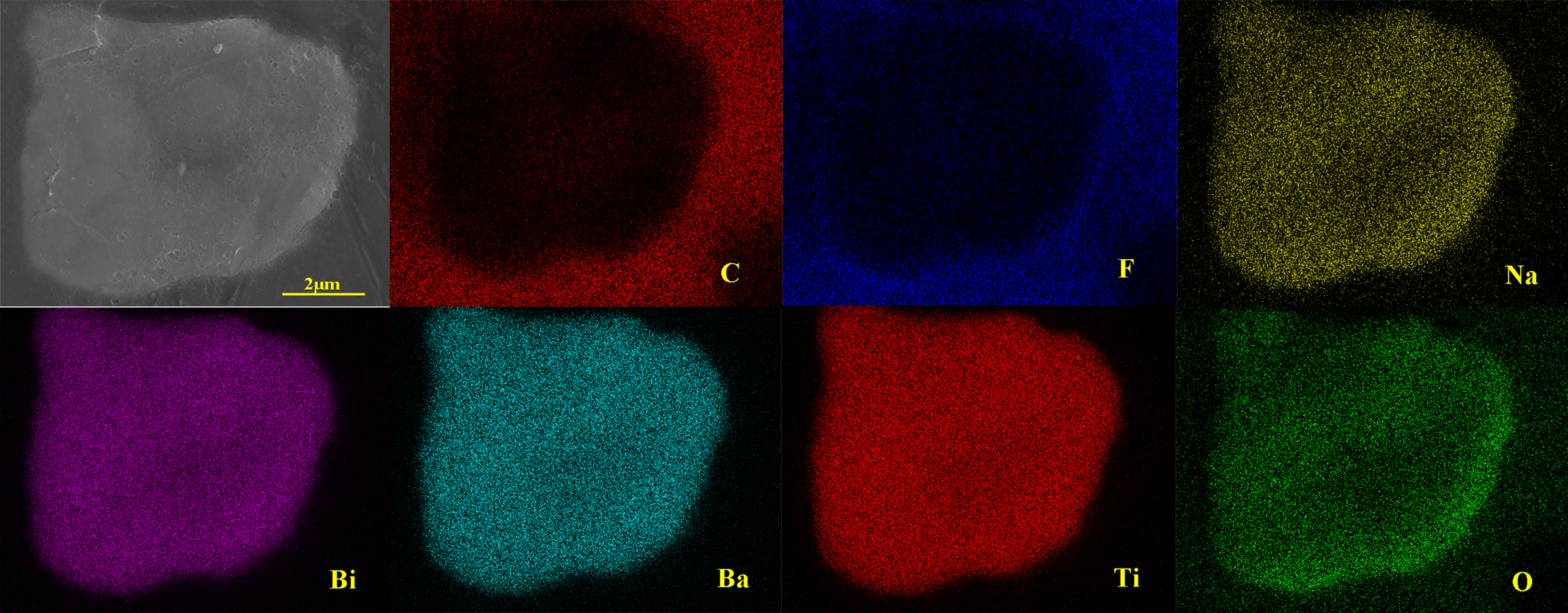
2μm
C
F
Na
Bi
Ba
Ti
O

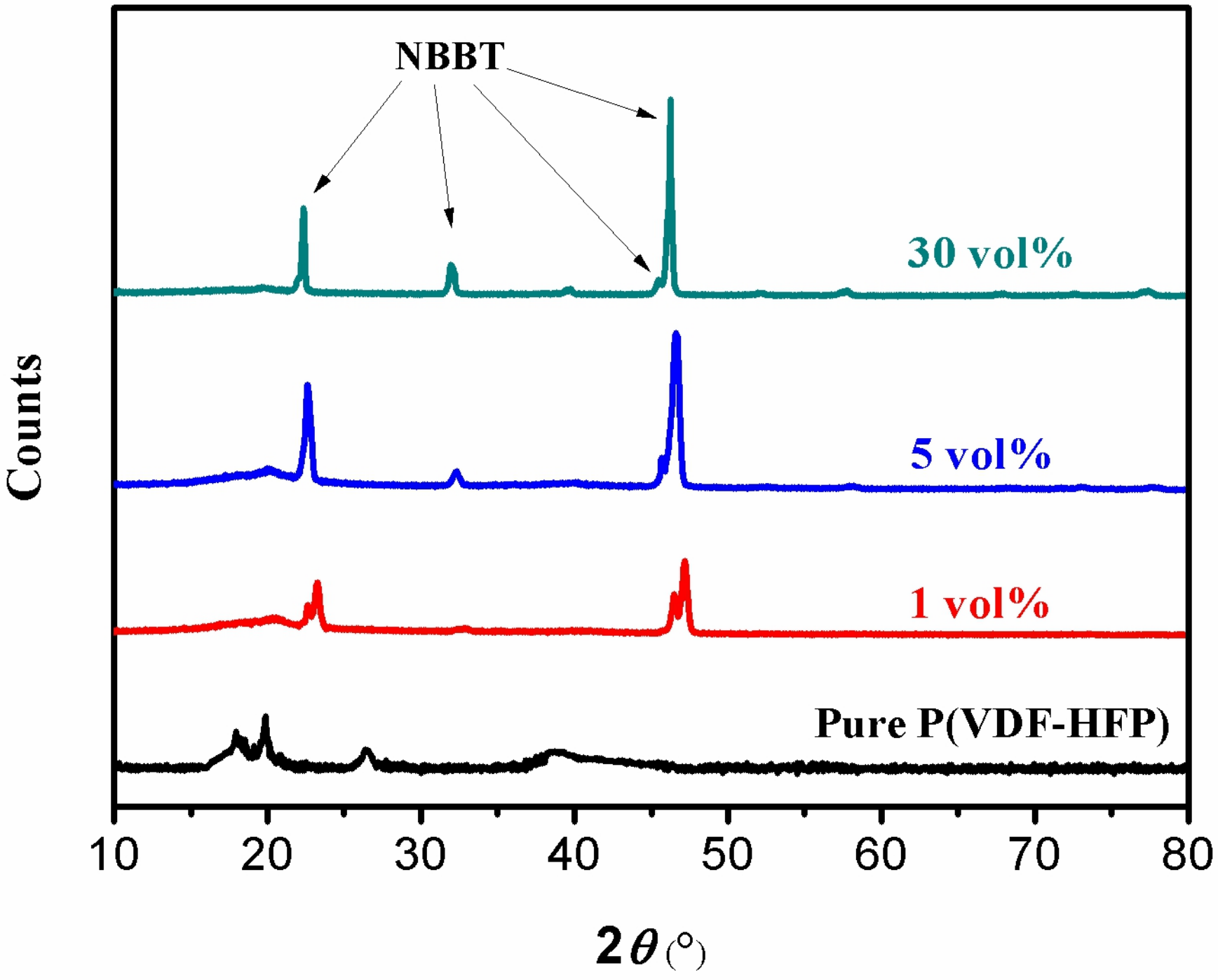
NBBT
30 vol%
5 vol%
1 vol%
Pure P(VDF-HFP)
Counts
10
20
30
40
50
60
70
80
2θ (°)

(a)

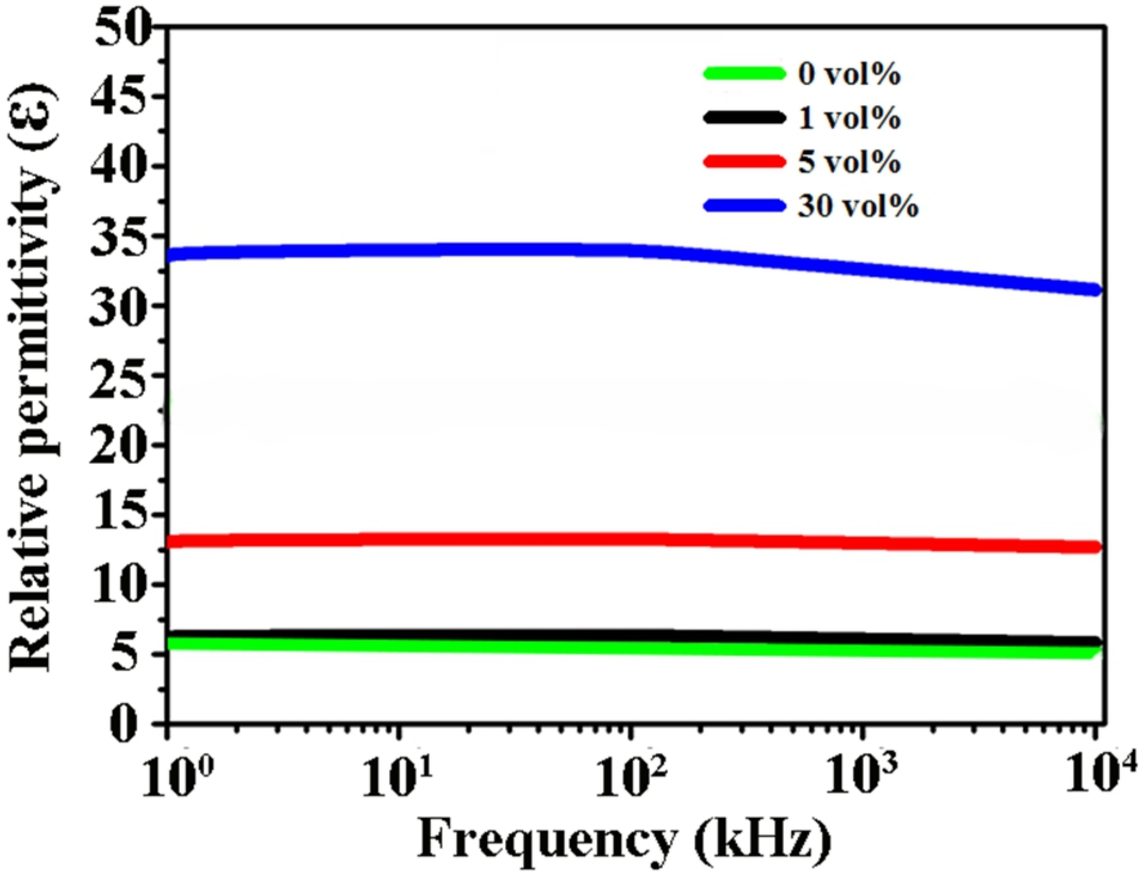
Relative permittivity (ε)
Frequency (kHz)
0 vol%
1 vol%
5 vol%
30 vol%

(b)

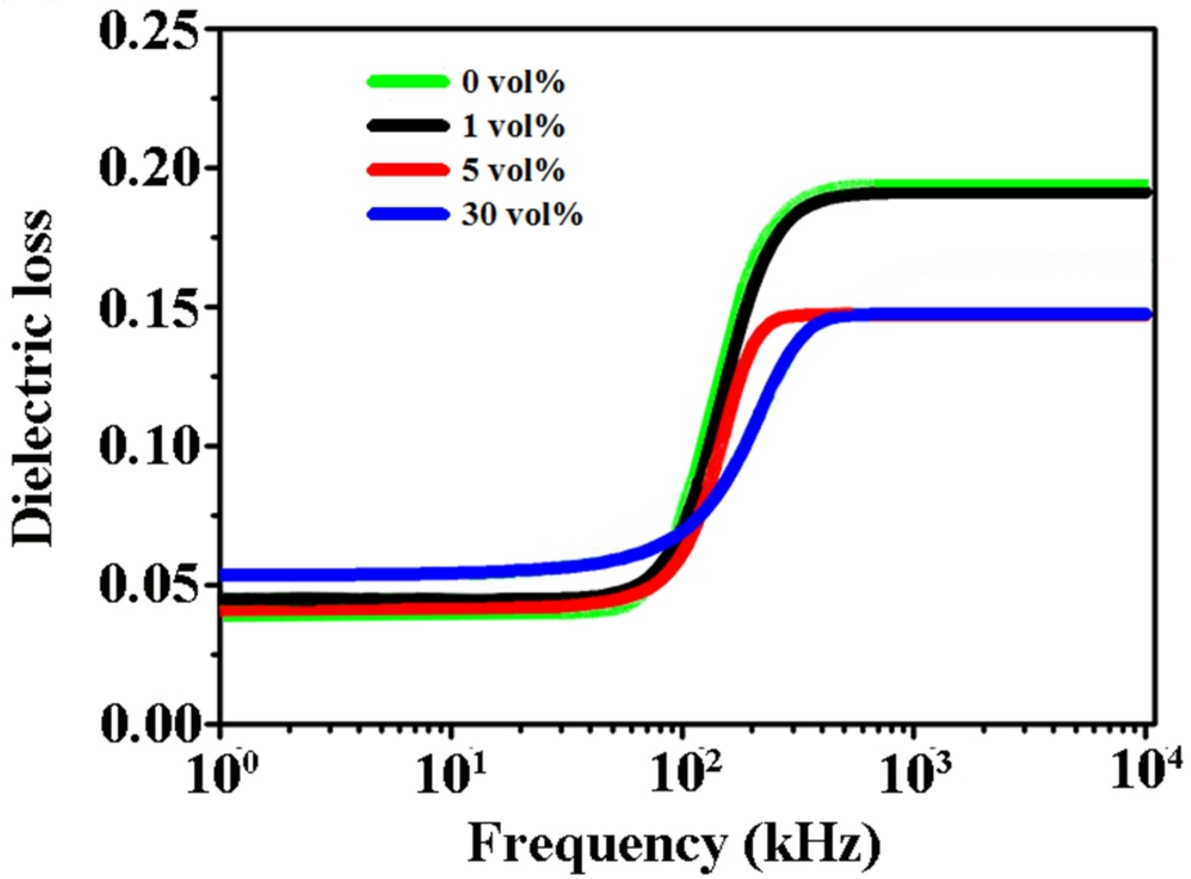
Dielectric loss
Frequency (kHz)
0 vol%
1 vol%
5 vol%
30 vol%

(c)

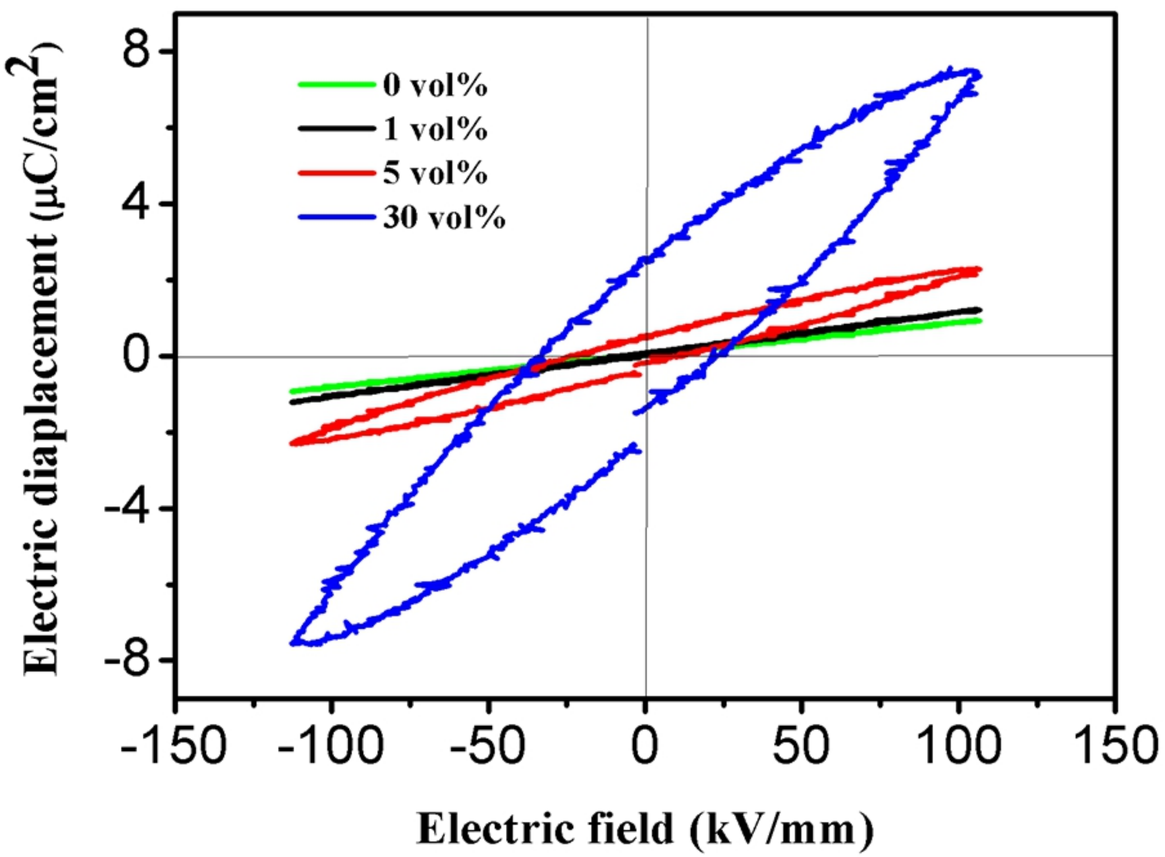
Electric diaplacement (μC/cm²)
Electric field (kV/mm)
0 vol%
1 vol%
5 vol%
30 vol%

(d)

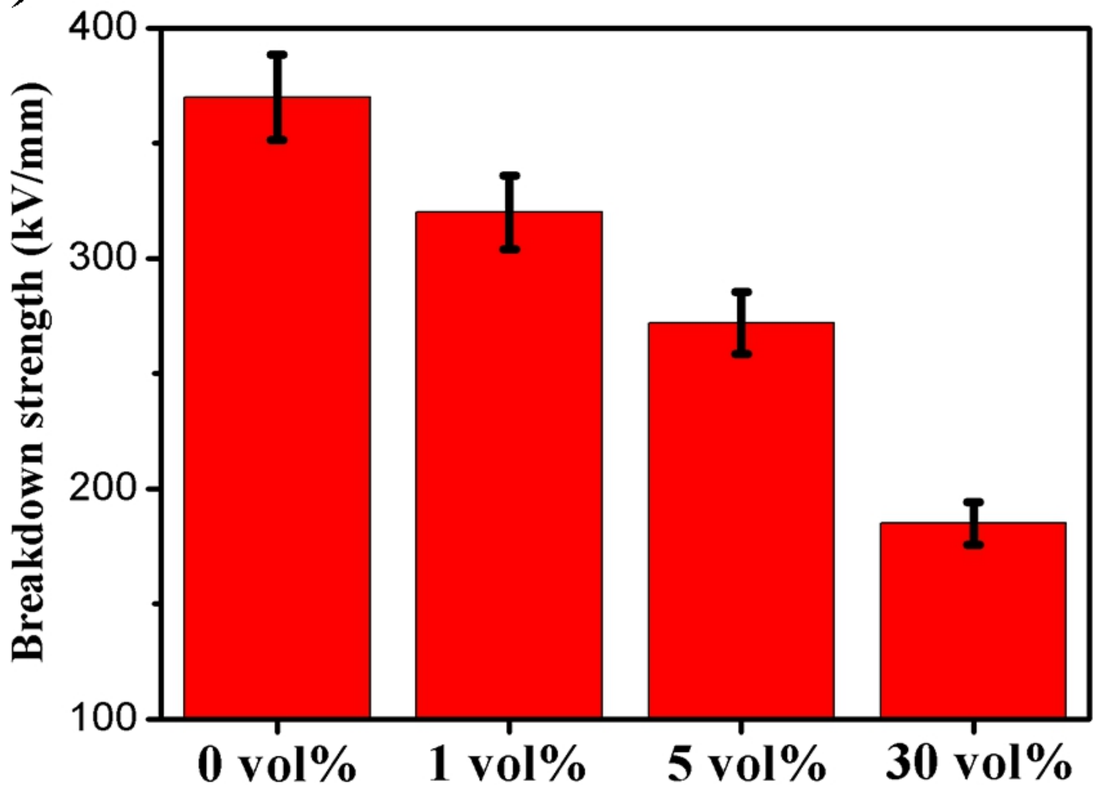
Breakdown strength (kV/mm)
0 vol%
1 vol%
5 vol%
30 vol%

(a)

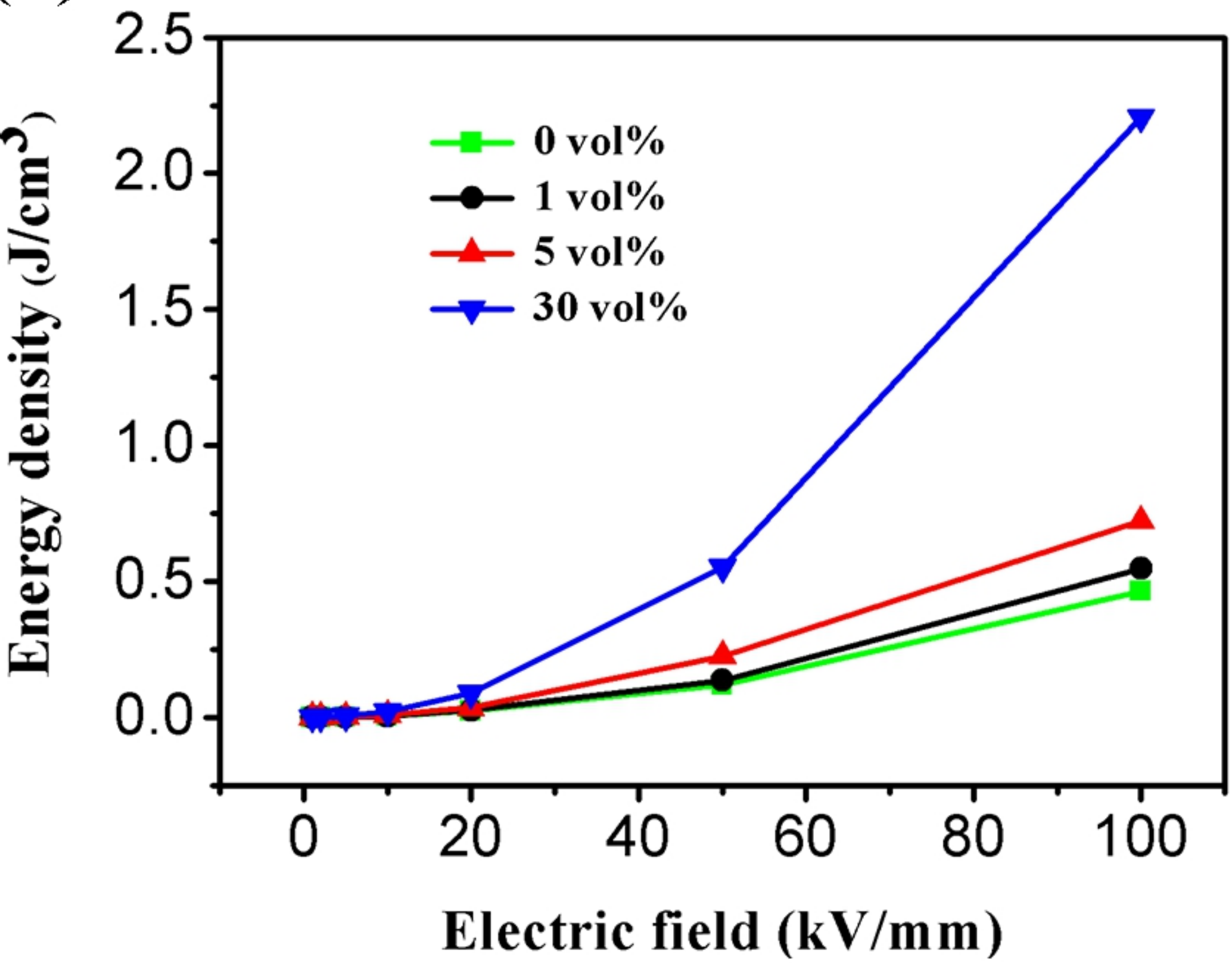
0 vol%
1 vol%
5 vol%
30 vol%
Energy density (J/cm3)
2.5
2.0
1.5
1.0
0.5
0.0
0
20
40
60
80
100
Electric field (kV/mm)

(b)

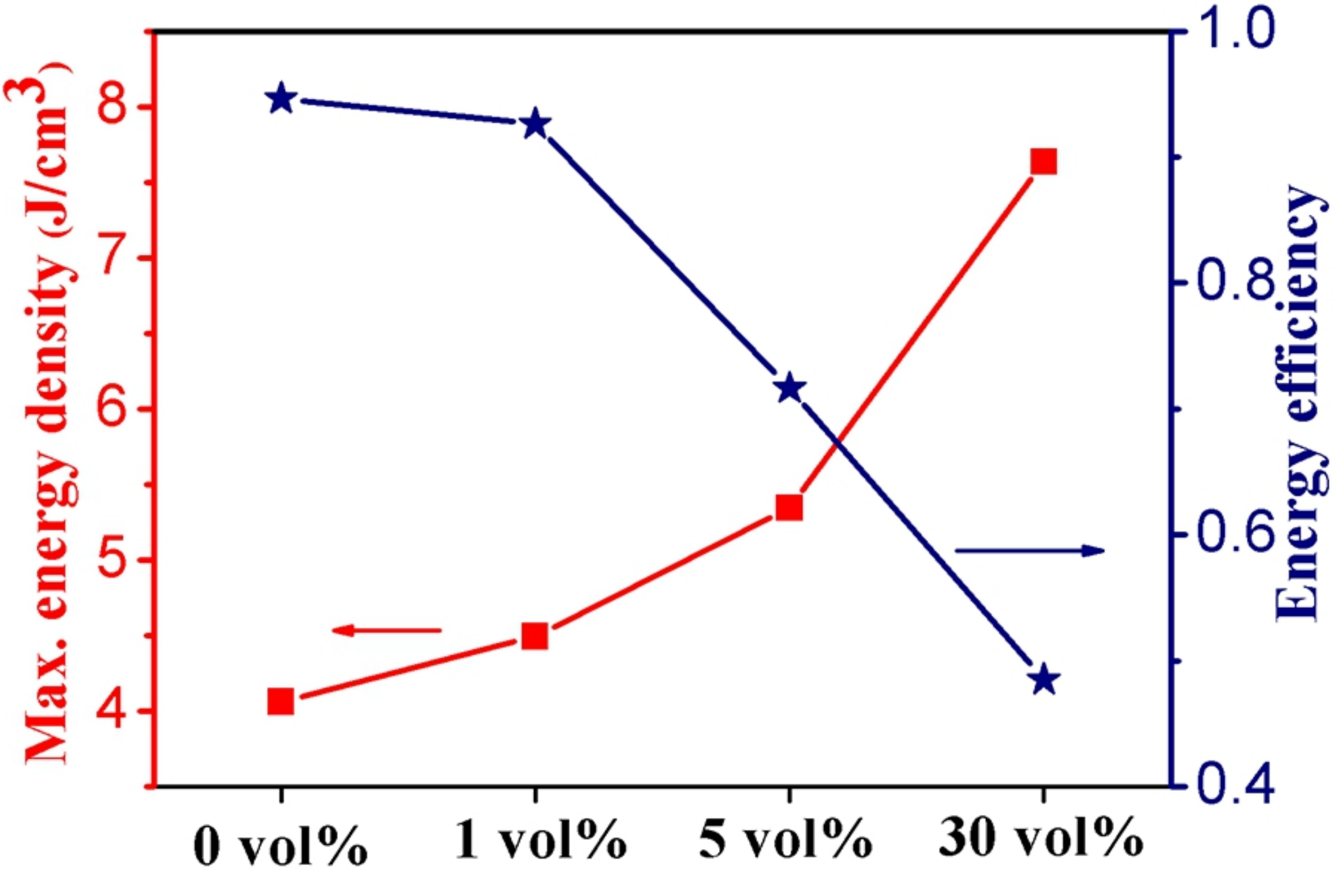
Max. energy density (J/cm3)
8
7
6
5
4
Energy efficiency
1.0
0.8
0.6
0.4
0 vol%
1 vol%
5 vol%
30 vol%

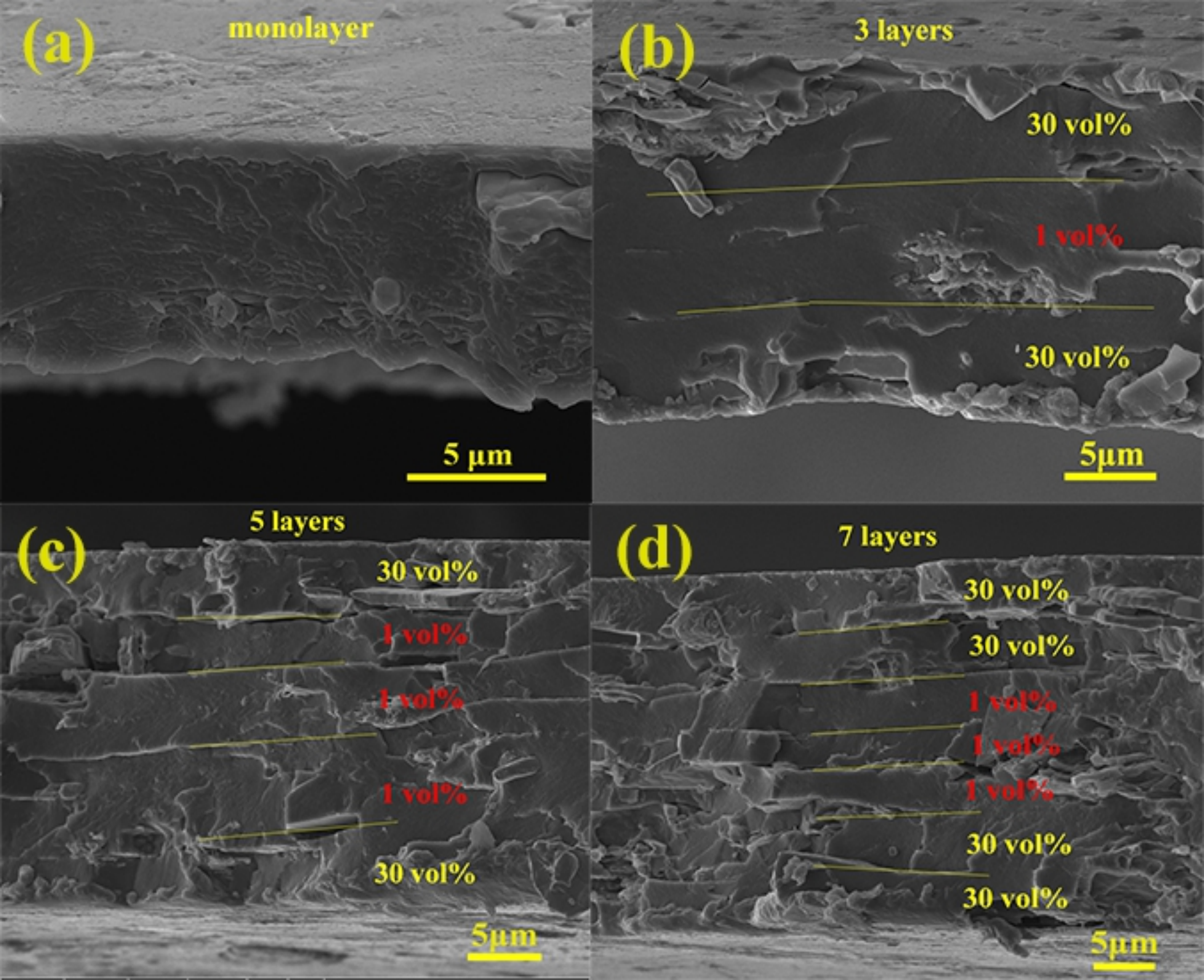
(a)
monolayer
5 µm
(b)
3 layers
30 vol%
1 vol%
30 vol%
5µm
(c)
5 layers
30 vol%
1 vol%
1 vol%
1 vol%
30 vol%
5µm
(d)
7 layers
30 vol%
30 vol%
1 vol%
1 vol%
1 vol%
30 vol%
30 vol%
5µm

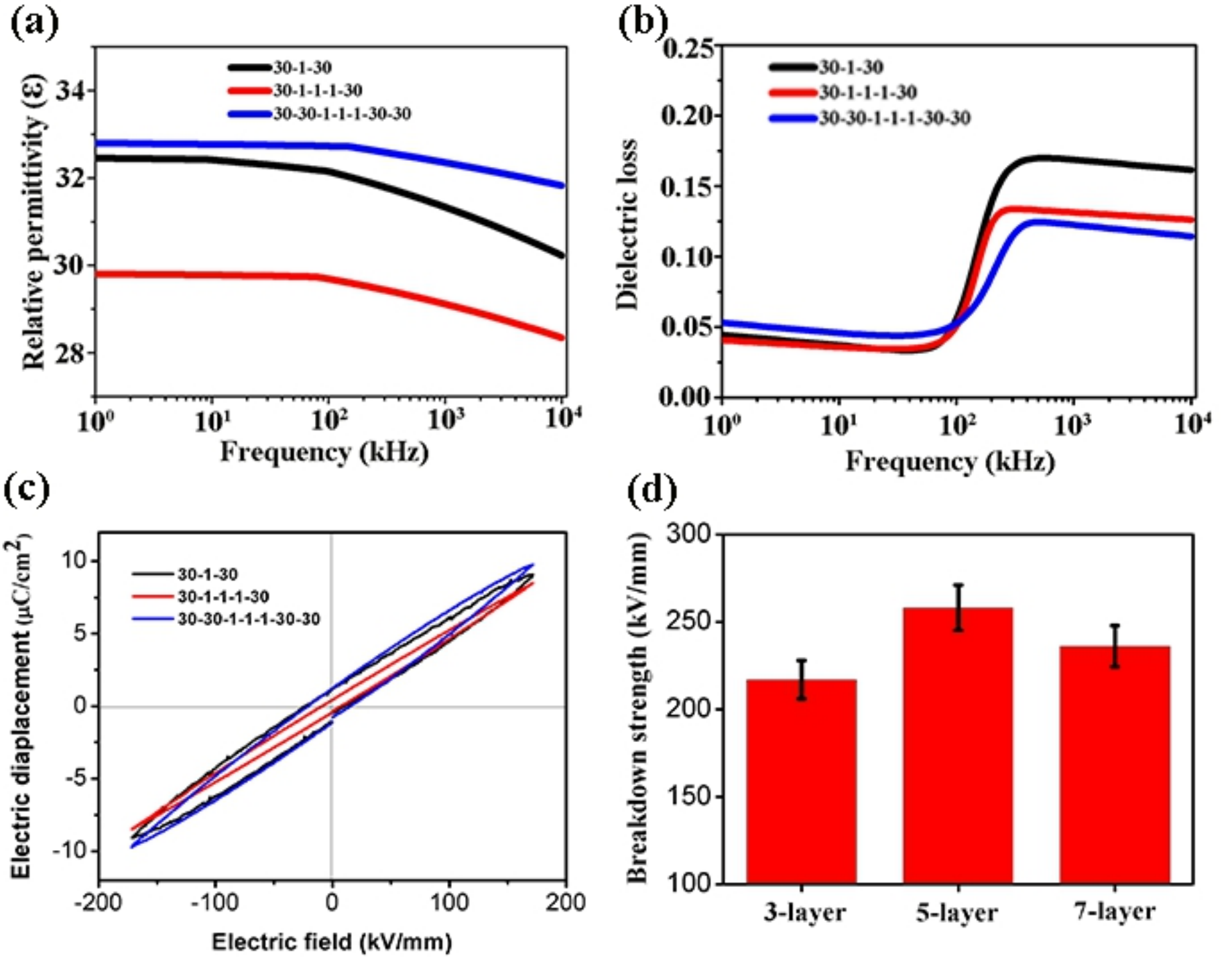
(a)
Relative permittivity (ε)
34
32
30
28
30-1-30
30-1-1-1-30
30-30-1-1-1-30-30
10^0
10^1
10^2
10^3
10^4
Frequency (kHz)
(b)
Dielectric loss
0.25
0.20
0.15
0.10
0.05
0.00
30-1-30
30-1-1-1-30
30-30-1-1-1-30-30
10^0
10^1
10^2
10^3
10^4
Frequency (kHz)
(c)
Electric diaplacement (μC/cm^2)
10
5
0
-5
-10
30-1-30
30-1-1-1-30
30-30-1-1-1-30-30
-200
-100
0
100
200
Electric field (kV/mm)
(d)
Breakdown strength (kV/mm)
300
250
200
150
100
3-layer
5-layer
7-layer

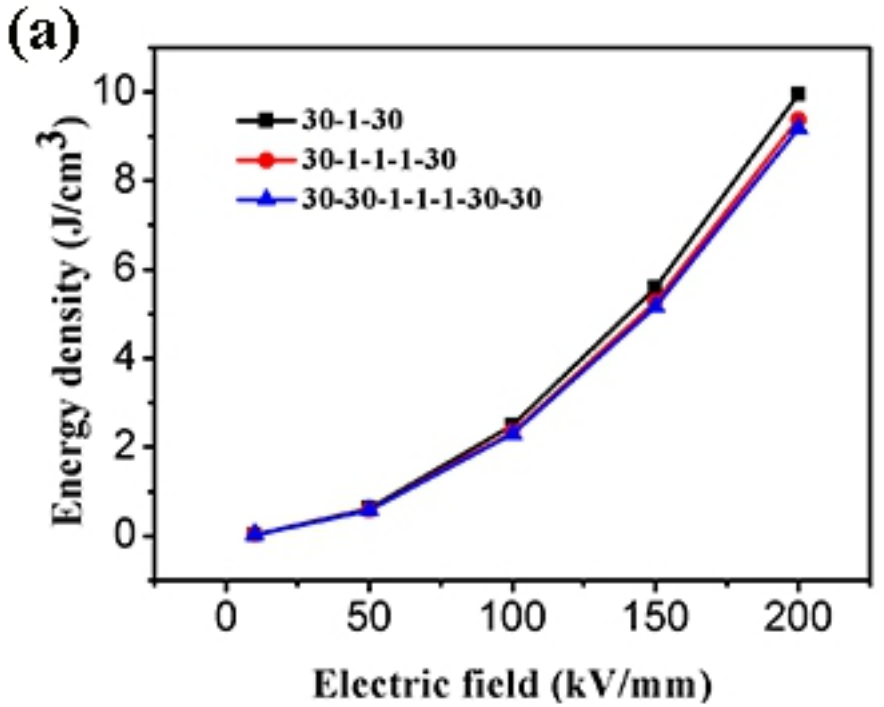
(a)
Energy density (J/cm3)
10
8
6
4
2
0
30-1-30
30-1-1-1-30
30-30-1-1-1-30-30
0
50
100
150
200
Electric field (kV/mm)

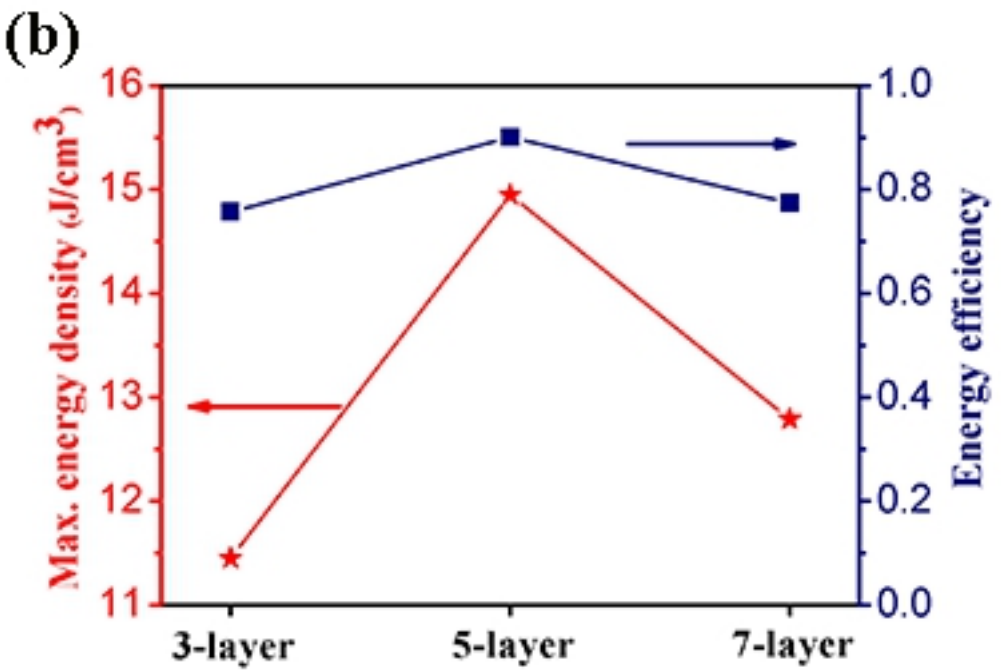
(b)
Max. energy density (J/cm3)
16
15
14
13
12
11
Energy efficiency
1.0
0.8
0.6
0.4
0.2
0.0
3-layer
5-layer
7-layer